*American Mineralogist, Volume 89, pages 1176–1182, 2004*

# Dynamics of trimethylene oxide in a structure II clathrate hydrate

**C. Y. JONES[1,*] AND I. PERAL[1,2]**

[1]NIST Center for Neutron Research, National Institute of Standards and Technology, Gaithersburg, Maryland 20899-8562, U.S.A.
[2]Department of Materials Science and Engineering, University of Maryland, College Park, Maryland 20742-2115, U.S.A.

## ABSTRACT

Neutron scattering has been used to study the dynamics of trimethylene oxide (TMO) in a structure II clathrate hydrate. Two regimes of guest dynamics have been identified in the range 10 K to 100 K. Below 50 K, the hydrogen atoms on TMO execute jumps between nonequivalent sites with a jump distance of 2.1 Å, consistent with a model of rotations of 90° about the $C_{2v}$ molecular axis between sites with unequal occupancy probabilities, and corresponding to an energy difference between sites of ~7 meV. Above 50 K, a second dynamical regime appears in which rotational motions of H occur about both the $C_{2v}$ axis and a second axis perpendicular to the plane of the molecule. An increase in the activation energy barrier to the motion that appears to accompany the onset of multi-axis motion could be a result of the additional high-energy rotations taking place within more restricted cross-sections of the cage.

## INTRODUCTION

Clathrate hydrates (CHs) exhibit unusual thermophysical properties when compared to ice. The large thermal expansivity (Tse et al. 1987), glasslike thermal conductivity (Tse and White 1988), and memory effect in pressure-amorphized hydrates (Handa et al. 1991) are attributed to the presence of the guest and its interaction with the host. In recent years, the glass-like thermal conductivity has attracted the most study, and has been shown by means of molecular dynamics (MD) simulations to result from the resonant scattering of acoustic phonons by localized guest vibrations (Baumert et al. 2003). The degree of success achieved so far from MD simulations in explaining the nature and mechanism of guest-host interaction has surpassed that of their experimental verification, especially regarding the phonon dispersion curves and guest dynamics.

The cyclic ether trimethylene oxide (TMO, $C_3H_6O$) has the unique ability to form both structure I (sI) and structure II (sII) frameworks (von Stackelberg 1958), depending on the composition of the initial mixture of TMO and water (Sargent and Calvert 1966; Hawkins and Davidson 1966; Gough et al. 1974; Davidson 1973). In sII CH, $C_3H_6O{\cdot}17H_2O$, TMO occupies the large ($5^{12}6^4$) cage, which has a mean free diameter of 6.6 Å (Sargent and Calvert 1966) and allows TMO, with a van der Waals diameter of 5.5 Å (Davidson 1973), enough room to undergo nearly unrestricted rotation. The ability of TMO to form both sI and sII CHs allows the investigation of its dynamics within two distinct cage environments; from a study of these dynamics, information may be provided regarding the environments themselves.

Rondinone et al. (2003) studied the structure of sII TMO CH as a function of temperature by constant wavelength neutron diffraction and found that the TMO does not exhibit preferred orientation in the range (10–250) K. However, the low-frequency dielectric permittivity, $\varepsilon_0$, of TMO in sII CH passes through a maximum in the range (25–55) K, and thus reflects an increasing degree of anisotropy in the guest motion, attributed to significant energy differences between various orientations with decreasing temperature (Gough et al. 1973). Bertie and Jacobs (1978) assigned two features in the far-infrared (IR) region at 21 and 34 $cm^{-1}$ as related to rotational vibrations involving reorientation of the dipole moment of TMO about two principal axes of inertia. Therefore, although TMO exists in a structurally disordered environment, its motions are anisotropic. In order to understand this aspect of CH behavior more fully on a microscopic level, a study of the dynamics of TMO itself is required.

This paper reports a study of the dynamics of TMO in a sII clathrate hydrate in the range 10–100 K, performed with the Disk Chopper Spectrometer (DCS) (Copley and Cook 2003), a time-of-flight cold neutron spectrometer at the National Institute of Standards and Technology Center for Neutron Research. From this study, the geometry, time scale, and energetics of the rotational motions of TMO in a $5^{12}6^4$ cage are described. Neutron scattering is well suited for the study of guest dynamics of clathrate hydrates; the large incoherent scattering cross-section of hydrogen produces an intense signal from TMO relative to that from deuterium and O atoms in the host. A comparison of the incoherent scattering originating from purely elastic scattering with the quasielastic component of scattering allows calculation of the *elastic incoherent structure factor* (EISF), which contains information about the geometry of the whole-molecule reorientations by way of the scattering intensity due to the motions of the H atoms. In addition, the width of the quasielastic component provides information regarding the time scale of the motions and its temperature dependence reveals the energetics of the associated activation process.

## EXPERIMENTAL METHODS

A polycrystalline sample of TMO sII clathrate hydrate ($C_3H_6O{\cdot}17D_2O$) was prepared following the procedure of Rondinone et al. (2003). The mass of sample used for the measurements was ~0.1 g, chosen to produce roughly a 10% scatterer

* E-mail: camille.jones@nist.gov

so as to minimize absorption and multiple scattering. To form a thin (~0.5 mm) annulus of frozen powder, the powdered sample was spread onto half of a rectangular sheet of consumer-grade aluminum foil, which was rolled tightly into a cylinder and placed into a cylindrical aluminum can (20 mm i.d., 100 mm high). The sample loading was performed over a liquid nitrogen bath inside a He-filled glove bag.

Neutron-scattering measurements were performed with the DCS with an incident wavelength of 4.8 Å resulting in an energy resolution of 0.120 meV full width at half maximum (FWHM). Neutrons were counted with 913 detectors spanning $-30° < 2\theta < 120°$. The neutron time-of-flight from the sample to the detector, $t_{SD}$, was measured across 1000 time channels in the range (1.5–10.5) ms, with a constant channel width of 0.009 ms. This experimental configuration yielded neutron energy transfer within the range –33 to 2.7 meV (energy loss) with a resolution of 0.118(5) meV, when only the first frame of neutron arrival times is considered. Six-hour measurements were performed at (10, 15, 25, 35, 50, 100) K.

## RESULTS

### Data reduction

Figure 1 is a plot of total neutron counts as a function of detector number (i.e., $Q$ or $2\theta$) and shows the location of elastic coherent (Bragg) scattering and confirms that the sample is of high purity; no reflections from ice I*h* were observed. Since only the incoherent scattering is relevant to the analysis described below, the detectors where elastic coherent scattering occurred were excluded from the analysis. Data reduction and analysis were performed with the Data Analysis and Visualization Environment (DAVE) standard routines developed at NIST. Raw data were corrected for time-averaged dark counts and for scattering from an empty aluminum can measured at 20 K. In general, the detector efficiency and attenuation factor were assumed to be unity. Detectors at the extremes of the detector bank were omitted to eliminate the necessity for vanadium standard normalization; the remaining detectors possess comparable efficiency and yielded spectra indistinguishable from those normalized to a vanadium standard. The remaining detectors were combined into ten groups in the range $0.19 < Q < 2.36$ Å$^{-1}$. The corrected data were converted to double differential scattering cross-sections, $S(Q,\omega)$, at each temperature. The $S(Q,\omega)$ were rebinned from 1000 constant-time increments in the range –33.805 to 2.78815 meV to 2000 constant-energy increments of 0.01829 meV over the same energy range. The uncertainty in the neutron velocity, $v_n$, increases with decreasing $v_n$, therefore the neutron-energy-loss portion of the spectrum from +0.5 to +3.3 meV contained a large degree of uncertainty and was not included in the analysis described below. The corrected $S(Q,\omega)$ are plotted in Figure 2.

### Analysis of spectra

The intensity of the elastic peak in $S(Q,\omega)$, shown inset in Figure 2, decreases with temperature and is accompanied by an increase in quasielastic broadening. The FWHM of the quasielastic components are independent of Q, therefore they provide evidence for a simple reorientational process taking place over a restricted number of sites, and that translational diffusion of TMO is not present. The FWHM of the elastic peak at 10 K is 0.120 meV, which is close to instrument resolution. Since essentially no broadening of the elastic peak occurs at 10 K, the data at this temperature were used as a resolution function, and a lower limit of 100 GHz may be estimated for the frequencies of the motions of TMO molecules in the cages.

Broad, weak inelastic features, shown in Figure 3, occur in the region of 1–30 meV (neutron energy gain) with maxima at approximately 2.3, 4.1, and 10 meV superimposed on quasielastic scattering. The feature at 10 meV is broad and faint and statistics are insufficient for its analysis. In the CH specimens studied, the guest is hydrogenated and the host is deuterated, therefore scattering from H dominates the spectrum and the observed inelastic features must originate from H in the guest molecule. Additional insight into the origin of the inelastic features is gained by comparison to the far-IR spectrum of sII TMO CH (Bertie and Jacobs 1978), in which broad features observed at 21 cm$^{-1}$ (2.6 meV) and 34 cm$^{-1}$ (4.2 meV) were assigned to rotational vibrations of TMO. The features observed in the far-IR spectrum are zone-center vibrations, but in neutron spectroscopy, an average over the entire Brillouin zone is observed. Spectra from the sI CH of methane show inelastic features at (8.3, 27, 60) meV, which MD simulations attribute to one rotational (8.3 meV) and two translational vibrations (Baumert et al. 2003). For the sI xenon CH, features calculated at 21, 33, and 52 cm$^{-1}$ occur due to translational vibrations (Tse et al. 1997). All of the available theoretical and experimental results support the conclu-

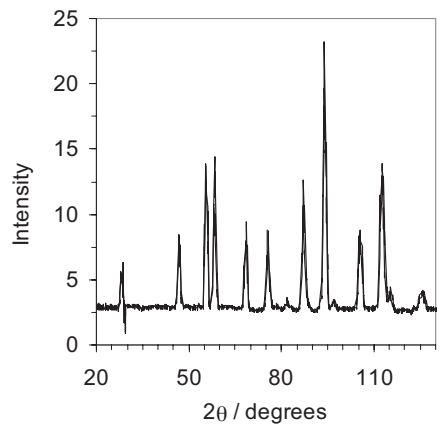


**FIGURE 1.** Trimethylene oxide sII clathrate hydrate on DCS, with incident neutrons of wavelength 4.8 Å. The sum of raw counts over all time channels is plotted against 2θ.

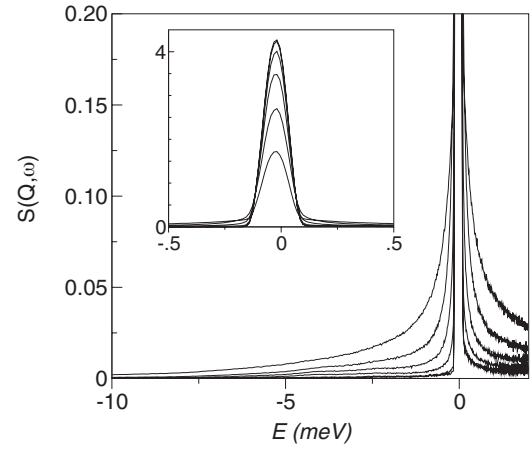


**FIGURE 2.** Corrected $S(Q,\omega)$ at (bottom to top trace; top to bottom in inset) 15, 25, 35, 50, and 100 K. The inset shows the elastic peaks at full scale.

sion that inelastic features at the lowest energies originate from rotational vibrations, and translational vibrations occurring at slightly higher energies. In light of these facts, it is reasonable to speculate that the features at 2.1 and 4.6 meV can be assigned to guest molecule vibrations. The intensities of these features were difficult to analyze due to their low intensity and proximity to increasing amounts of quasielastic scattering with temperature. For the analysis described below, it must be assumed that the inelastic features are localized in energy so that translational-rotational coupling may be disregarded.

The scattering observed in $S(Q,\omega)$ is dominated by the incoherent scattering cross-section of hydrogen, $\sigma_{inc}(H)$. For a hydrogenous TMO guest with no exchangeable protons enclathrated in a fully deuterated host, the ratio of $\sigma_{inc}(H)$ to the total cross sections of O, C, and $^2H$ (D) is 1.5, where the total cross-section is taken to be the sum of the coherent, incoherent, and absorption cross-sections. The ratio of $\sigma_{inc}(H)$ to the sum of the incoherent and absorption cross sections for O, C, and $^2H$ (D) is 7. Deuterium only contributes to the elastic scattering, since the reorientational motion of $D_2O$ molecules in the host takes place on the order of kilohertz (Tse et al. 2001), so that on the time scale of this experiment the water molecules in the host exist in a statically disordered state. Moreover, the majority of the coherent scattering is in the Bragg reflections, which were omitted from the analysis. Therefore, the experimentally derived $S(Q,\omega)$ is to a good approximation the incoherent scattering function

$$S_{inc}(Q,\omega) = e^{-2W}[A_o(Q)\delta(\omega) + S^{qel}{}_{inc}(Q,\omega)] + S^{M}{}_{inc}(Q,\omega) + S^{I}{}_{inc}(Q,\omega) \quad (1)$$

where $e^{-2W}$ is the Debye-Waller factor and $A_o(Q)\delta(\omega)$ represents the purely elastic part of the scattering function. The term $S^{qel}{}_{inc}(Q,\omega)$ represents the quasielastic component and is a measure of the Doppler broadening of the elastic line due to the rotation of the H atom about the center of mass of TMO. The term $S^{M}{}_{inc}(Q,\omega)$ is the multiple-scattering contribution, which has been neglected owing to the sample size. $S_{inc}(Q,\omega)$ is dominated by H, the contribution of which is 7 times as large as that from D. For convenience, $S_{inc}(Q,\omega)$ can be separated into purely elastic and inelastic terms, obtained from the Fourier transform (FT) of the space-time self-correlation function, $I_{inc}(Q,t)$, split into its time-dependent and time-independent parts (Bée 1988; Bée 1992). The coefficient of the purely elastic term of $S_{inc}(Q,\omega)$, called the elastic incoherent structure factor (EISF), is the space-FT of final distribution of scattering nuclei averaged over all initial positions. Additionally, if $S_{inc}(Q,\omega)$ is integrated over all $\omega$ at constant $Q$, the value obtained is unity, i.e., EISF is equal to the fraction of the incoherent intensity contained in the purely elastic peak. EISF is therefore approximated by an experimental EISF value obtained from the integrated areas of the elastic and quasielastic portions of the spectrum:

$$\text{EISF} = \frac{I_{elas}(Q)}{I_{elas}(Q) + I_{quasi}(Q)} \quad (2)$$

where $I_{elas}(Q)$ and $I_{quasi}(Q)$ are the integrated intensities of the elastic and quasielastic components of the spectrum at a given $Q$. Integration of the elastic and quasielastic peaks was performed by a typical procedure of fitting the spectrum to a weighted sum of two functions, a delta function to describe the elastic scattering and a Lorentzian to describe the quasielastic portion, both functions being convoluted with the 10 K experimental resolution function.

The experimental EISFs are plotted in Figure 4. Most prominent in the EISFs are a diminishing intensity with increasing temperature and a shift of the minima of the curves to lower values of $Q$, also with increasing temperature. The former change indicates an increase in the motion of TMO as temperature increases, and the latter is a clear indication of a change in the length scale of the motion at higher temperatures.

## Modeling the EISF

As shown in Figure 4, the experimental EISF [denoted $A_o(Q)$ to indicate a specific dynamical model] is not adequately described by a model for isotropic rotational diffusion without the introduction of temperature-dependent variables, as given by

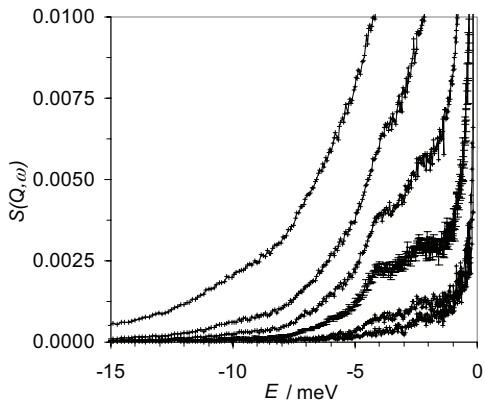


**FIGURE 3.** Inelastic scattering at (bottom to top trace) 10, 15, 25, 35, 50, and 100 K. The 25 K trace is shown with error bars indicating a relative uncertainty of 5%, which is the mean relative uncertainty in the range –15 to 1 meV.

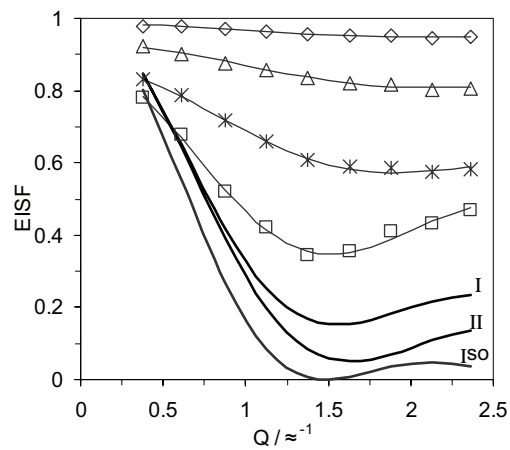


**FIGURE 4.** Experimental EISFs at (top to bottom) 25 (stars), 35 (triangles), 50 (astericks), and 100 K (boxes). The thin, solid lines drawn through the points are from fits of Equation 12 to the experimental EISFs. For comparison, model calculations with models I, II, and isotropic rotational diffusion (Iso) with r = 1.5 Å have been included.

$$A_o(Q) = a_1 j^2_o(Qr) + a_2 \quad (3)$$

In Equation 3, $a_1$, and $a_2$ represent temperature-dependent variables to account for a static contribution and an additional $Q$-dependence, respectively, $j_0$ is a zero-order spherical Bessel function of the first kind, and $r$ is the radial distance from the center of mass of TMO to the H atom involved in the rotational motion of interest. For purely isotropic rotational diffusion, $a_1 = 1$ and $a_2 = 0$, however, Equation 3 describes the experimental EISFs at 25 and 35 K only if $a_1$, $a_2$, and $r$ are all included as functions of temperature. Given the anisotropic nature of the motion as indicated by the EISFs, it therefore becomes necessary to consider a model to describe this anisotropy, most conveniently in terms of rotation about a principal axis of TMO in an arbitrary orientation within the cage. Refinements of neutron diffraction data for sI TMO CH indicate that the $C_{2v}$ axis[13] (Creswell 1975) of TMO is oriented along the $\bar{4}$ axis of the cage. Given the structural similarities between sI and sII CHs, it is reasonable to consider that TMO in sII CH may possess a tendency to preferred orientation along the $\bar{4}$ axis in the $5^{12}6^4$ cage. Such a model of TMO in the $5^{12}6^4$ cage, with the $C_{2v}$ axis[13] of TMO along the $\bar{4}$ axis of the cage, is depicted schematically in Figure 5.

A single-axis jump model for rotation about the $\bar{4}$ axis yields the EISF given by Yildirim et al. (1999):

$$A_o(Q) = \frac{1}{3} + \frac{2}{3}\sum_{i=1}^{2}\sum_{j=1}^{2} P_i P_j j_o(Q\sqrt{2}r) \quad (4)$$

where $P_i$ is the occupancy probability for an H at site $i$. At 25 and 35 K, rotations of 90° about the $C_{2v}$ molecular axis between two sites with unequal occupancy probabilities are sufficient to describe the EISF. For TMO, the jump distance between H sites separated by 90° is $r\sqrt{2}$, where $r$ obtained from a fit to the experimental EISF is 1.5(1) Å. This distance agrees with the mean distance from the center of mass of TMO to the H atoms. Given $r = 1.5$ Å, the jump distance for H is 2.1 Å. The occupancy probabilities, $P_i$, are listed in Table 1. Although the EISF should approach unity at the low-Q limit, and $P_1 + P_2$ should be equal to unity, the departures from unity were not deemed to be detrimental to the analysis; however, the estimates of the errors on $P_i$ are increased by one order of magnitude to take into account the departure of their sum from unity. Based on $P_i$, the energy difference between the two sites is estimated to be 8 meV at 25 K and 7 meV at 35 K.

At 50 and 100 K, the EISF cannot be described solely by rotations of 90° about the $C_{2v}$ molecular axis. At elevated temperatures, rotations may occur about more than one principle axis of TMO. For correlated jumps of $2r$ and $r\sqrt{2}$ about perpendicular axes, the EISF can be written

$$A_o(Q) = c_o + c_1 j_o(Q\cdot 2r) + c_2 j_o(Q\sqrt{2}r) \quad (5)$$

where $c_0$, $c_1$, and $c_2$ are temperature-dependent parameters, listed in Table 2, obtained from fits to the experimental EISFs. As shown in Figure 4, Equation 5 satisfactorily describes the EISFs at 50 and 100 K. The sum $c_0 + c_1 + c_2$ is expected to be unity; however, in the present analysis, this sum is 0.87. This departure from unity may be due to the presence of inelastic or multiple scattering.

At 50 K, which corresponds to $kT \sim 6$ meV, and at 100 K ($kT \sim 12$ meV), the thermal energy of the system is on the order of the activation energies obtained at 25 and 35 K. At these lower temperatures, the possible H sites are still inequivalent because the thermal energy present in the system is not sufficient to overcome the potential energy barriers present in the $5^{12}6^4$ cage. However, as $T$ increases, the thermal energy present in the system allows H to populate a number, $n$, of equivalent sites by means of rotations of TMO. One way of describing the ability of H to populate $n$ equivalent sites is to calculate the EISF for molecular jumps among twelve crystallographically equivalent sites related by the point symmetry, 23, of the molecule within the cage at coordinates (3/8, 3/8, 3/8).

The formalism, based on group theoretical methods (Rigny 1972), assumes that for a well-defined rotation belonging to class μ, the probability per unit time is $1/\tau_\mu$, where $\tau_\mu$ is the average time between two successive jumps for rotations within class μ. If $n_\mu$ is the number of rotations in class μ, then the characteristic time, $\tau_\alpha$, associated with the irreducible representation $\Gamma^{(\alpha)}$ is given by

$$\frac{1}{\tau_\alpha} = \sum_\mu \frac{n_\mu}{\tau_\mu}\left(1 - \frac{\chi^\mu_\alpha}{\chi^E_\alpha}\right) \quad (6)$$

where E is the identity operation. From the appropriate character table, shown in Table 3, the relevant correlation times can be evaluated. Given the assumption that the probability of any rotation of π/3 (or 2π/3) is equal to that of a rotation of –π/3 (–2π/3), two jump probabilities, $1/\tau(C_{3j})$ and $1/\tau(C)$, are defined. From Equation 6, the relevant jump rates have been calculated and are listed in Table 4.

With the jump rates defined above, the intermediate rotational scattering function can be expressed as:

**TABLE 1.** Occupancy probabilities for jump model involving two inequivalent sites*

| | 25 K | 35 K |
|---|---|---|
| $P_1$ | 0.02(2) | 0.09(1) |
| $P_2$ | 0.98(2) | 0.91(1) |
| $\Delta E$ (meV) | 8(2) | 7(1) |

*Notes:* The errors in parentheses are those estimated from the deviation of $P_1+P_2$ from unity; the true statistical uncertainties are one order of magnitude smaller.

* $\Delta E = \left(\frac{T}{11.604}\right)\mathrm{Ln}\left(\frac{P_2}{P_1}\right)$

**TABLE 2.** Values of the fitted parameters versus temperature for the experimental EISF at 50 and 100 K as described by Eq. 8

| Parameter | 50 K | 100 K |
|---|---|---|
| $c_0$ | 0.614(1) | 0.437(1) |
| $c_1$ | 0.076(5) | 0.414(5) |
| $c_2$ | 0.176(4) | 0.020(1) |
| $r$ | 1.500 | 1.500 |
| $c_o+c_1+c_2$ | 0.87 | 0.87 |

*Note:* The radius of motion r is an input parameter.

**TABLE 3.** Character table for the crystallographic point group 23(T)

| 23(T) | $E$ | $C_{2m}$ | $C_{3j}^+$ | $C_{3j}^-$ |
|---|---|---|---|---|
| $\Gamma_1$ (A1) | 1 | 1 | 1 | 1 |
| $\Gamma_2$ ($^1$E) | 1 | 1 | ω | ω* |
| $\Gamma_3$ ($^2$E) | 1 | 1 | ω* | ω |
| $\Gamma_4$ (T) | 3 | –1 | 0 | 0 |

$$I_{inc}^{R}(Q,t) = \sum_{\alpha} A_{\alpha}(Q)\mathrm{e}^{-(t/\tau_{\alpha})} \tag{7}$$

with the elastic and quasielastic structure factors given by:

$$A_{\alpha}(Q) = \frac{1}{N}\sum_{i=1}^{N}\left[\frac{\chi_a^{\mathrm{E}}}{g}\sum_{\mu}\sum_{\rho(\mu)}\chi_a^{\mu} j_0\left(Q(\boldsymbol{r}^i - \rho(\mu)\cdot\boldsymbol{r}^i)\right)\right] \tag{8}$$

averaged over all directions of $\boldsymbol{Q}$, where $N$ is the number of H atoms in the molecule and $g$ is the order of the group.

Considering the jump rates above, three models can be envisaged corresponding to the occurrence, or lack, of particular rotations. It is convenient to define the following expressions to simplify the final form of the EISF models:

$$r_{\rho(\mu)}^{i} = \left|\boldsymbol{r}^i - \rho(\mu)\cdot\boldsymbol{r}^i\right| \tag{9}$$

$$A = \frac{1}{N}\sum_{i=1}^{N}\sum_{\rho(C_{2m})} j_0\left(Qr_{\rho(C_{2m})}^{i}\right) \tag{10}$$

$$B = \frac{1}{N}\sum_{i=1}^{N}\sum_{\rho(C_{3j}^{+})} j_0\left(Qr_{\rho(C_{3j}^{+})}^{i}\right) = \frac{1}{N}\sum_{i=1}^{N}\sum_{\rho(C_{3j}^{-})} j_0\left(Qr_{\rho(C_{3j}^{-})}^{i}\right) \tag{11}$$

Given orientation of the molecule along the $\overline{4}$ axis of the $5^{12}6^4$ cage, the jump distances listed in Table 5 are obtained.

For one model, designated Model I, we consider that both $C_3$ and $C_2$ rotations occur; therefore $1/\tau(\Gamma_2)$, $1/\tau(\Gamma_3)$, and $1/\tau(\Gamma_4)$ are not equal to zero, and

$$\mathrm{EISF_I} = \frac{1}{12}\left[1 + A + 2B\right] \tag{12}$$

For Model II, only $C_2$ rotations occur, therefore $1/\tau(\Gamma_2) = 1/\tau(\Gamma_3) = 0$ and $1/\tau(\Gamma_4) \neq 0$:

$$\mathrm{EISF_{II}} = \frac{1}{4}\left[1 + A\right] \tag{13}$$

Figure 5 shows the experimental and calculated EISFs and the EISFs calculated for group-theoretical Models I and II. As temperature increases, the experimental EISF approaches Models I and II, with good agreement of the minima in the functions. However, the temperature effect on rotations of the molecule among all the possible orientations given by the symmetry of the cage is inadequate to describe the experimental EISF. One possible explanation for this discrepancy is that not all of the $n$ orientations are equally probable.

**TABLE 4.** Relevant jump rates

| Term | Value |
|---|---|
| $\frac{1}{\tau(\Gamma_1)}$ | 0 |
| $\frac{1}{\tau(\Gamma_2)}$ | $\frac{16}{\tau_{C_{3j}}}$ |
| $\frac{1}{\tau(\Gamma_3)}$ | $\frac{16}{\tau_{C_{3j}}}$ |
| $\frac{1}{\tau(\Gamma_4)}$ | $\frac{4}{\tau_{C_{2m}}} + \frac{8}{\tau_{C_{3j}}}$ |

**TABLE 5.** Jump distances of hydrogen in Ångstroms for rotations of TMO about (3/8,3/8,3/8), from the initial coordinates (x,y,z) expressed in the crystallographic system

| ρ(μ) | $r_{\rho(\mu)}^{1}$ | $r_{\rho(\mu)}^{2}$ | $r_{\rho(\mu)}^{3}$ | $r_{\rho(\mu)}^{4}$ | $r_{\rho(\mu)}^{5}$ | $r_{\rho(\mu)}^{6}$ |
|---|---|---|---|---|---|---|
| x,y,z | 0 | 0 | 0 | 0 | 0 | 0 |
| x+3/4,y+3/4,z | 2.84066 | 3.21818 | 2.19235 | 3.14681 | 4.35832 | 2.01613 |
| x,y+3/4,z+3/4 | 3.41894 | 3.03873 | 2.94952 | 0.867853 | 4.36788 | 3.64467 |
| x+3/4,y,z+3/4 | 3.45871 | 1.4317 | 3.41894 | 3.03434 | 0.322932 | 3.09071 |
| z , x, y | 0.555176 | 2.23202 | 3.07304 | 2.46361 | 2.93919 | 1.63463 |
| y , z, x | 0.555176 | 2.23202 | 3.07304 | 2.46361 | 2.93919 | 1.63463 |
| −z+3/4,x+3/4,y | 3.16883 | 2.80257 | 2.41132 | 2.00171 | 3.01912 | 2.17483 |
| −y+3/4,z+1/2, −x+1/4 | 3.16883 | 2.80257 | 2.41132 | 2.00171 | 3.01912 | 2.17483 |
| z,-x+3/4,−y+3/4 | 3.1387 | 2.5876 | 2.94362 | 1.82931 | 3.22779 | 3.08659 |
| −y+3/4,−z+3/4,x | 3.1387 | 2.5876 | 2.94362 | 1.82931 | 3.22779 | 3.08659 |
| −z+3/4,x,−y+3/4 | 3.39411 | 1.452 | 1.12795 | 2.53775 | 3.16307 | 3.15784 |
| y,−z+3/4,−x+3/4 | 3.39411 | 1.452 | 1.12795 | 2.53775 | 3.16307 | 3.15784 |

## DISCUSSION

Two regimes of guest dynamics have been identified in the sII TMO clathrate hydrate in the range 10–100 K. Below 50 K, a model involving rotation about a single axis, about which the hydrogen atoms on TMO execute 90° jumps between inequivalent sites, satisfactorily reproduces the EISFs. The energy differ-

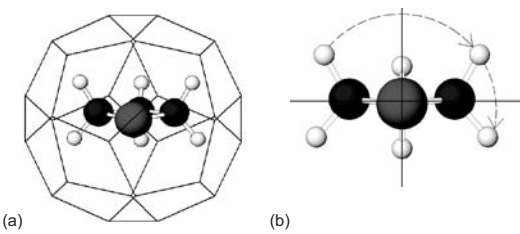


**FIGURE 5.** (**a**) TMO at fractional coordinates (3/8, 3/8, 3/8) in the $5^{12}6^4$ cage of sII CH, with the principal molecular ($C_{2v}$) axis of TMO along the fourfold rotation-inversion axis of the cage (perpendicular to the page); (**b**) position of H after two successive 90° rotations about

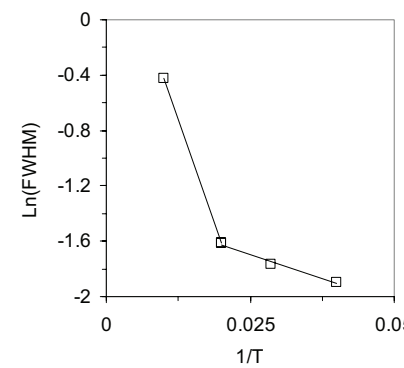


**FIGURE 6.** Plot of the log of the quasielastic FWHM vs. $1/T$. The four data points are (right to left) 25, 35, 50, and 100 K. Activation energies estimated from the slopes are 1.2 meV (25–50 K) and 7.7 meV (50–100 K).

ence between sites separated by 90°, estimated from occupancy probabilities listed in Table 1, is ~7 meV. Above 50 K, a second dynamical regime appears in which rotational motions of H occur about more than one axis. This result is not surprising, since the activation energy barriers encountered by the guest are very low. An activation energy of ~1.2 meV can be estimated from a plot of the log of the quasielastic FWHM vs. $1/T$, shown in Figure 6. This activation energy corresponds to ~14 K, thus the TMO encounters a low barrier to rotation from the confining cage potential. However, an increase in the energy barrier to the motion appears to accompany the onset of multi-axis motion; this could be a result of the additional high-energy rotations taking place within more restricted cross-sections of the cage.

That a change in the dynamical behavior of TMO in a sII CH occurs below 50 K is supported by both calorimetric and dielectric studies. Kuratomi et al. (1992) observed an exothermic peak in the heat capacity of sII CH of TMO at 30 K and an endotherm around 34.5 K in the direction of increasing temperature. They attributed the former peak to an irreversible transformation involving the onset of orientational order of TMO from a supercooled disordered state, and the latter to the corresponding reversible first-order phase transformation with a transformation entropy of 2.36 J/K. In addition, dielectric relaxation studies of KOH-doped sII TMO CH show relaxation below 35 K that is attributed to a persistence of orientational mobility of TMO, which was thought to occur because the van der Waals diameter of TMO is not large enough to introduce any significant steric constraints (Yamamuro et al. 1993). However, the fact that $\varepsilon_0$ of TMO in sII CH passes through a maximum (Gough et al. 1973) could also reflect an increasing energy difference between rotations about different axes, rather than or in addition to anisotropy in the guest motion caused by an increase in the energy difference between various orientations within the cage.

Comparison of these results to far-IR results published for TMO sII CH, and to experimental and computational results for sI methane and xenon hydrates suggests that the observed inelastic features are associated with rotational vibrations. However, a question that arises is whether translational modes can be observed for TMO. Comparisons to the behavior of sI CHs for which translational modes have been observed are of limited value, since TMO lacks the spherical symmetry of the other guests. Considering that translational modes are involved in the mechanism of the low thermal conductivity of CHs, calculations of the expected translational energies and measurement of the thermal conductivity of the sII TMO CH itself would help clarify the results presented here.

Although it has been established that a change in the dynamical behavior of TMO occurs around 50 K, there are some unresolved issues as to the nature of the orientational mobility present in the high and low-temperature regimes. The low-frequency dielectric permittivity, $\varepsilon_0$, of TMO in a sII CH in the range 55–200 K indicates that the guests undergo isotropic reorientation on a time scale of milliseconds; $\varepsilon_0$ decreases roughly as $1/T$, and also as the square root of the dipole moment of the guest (Gough et al. 1973). However, from the present study it is clear that TMO does not execute a purely isotropic rotational diffusion. Unfortunately, there are no structural clues as to the nature of the dynamical behavior of TMO in sII, as there are for sI CH, since the temperature dependence of the sII $5^{12}6^4$ cage volumes is roughly the same for guests of various sizes and polarities (Chakoumakos et al. 2003) and reflects the presence of ample room in the cage and thus minimal guest-host interactions.

TMO is an asymmetric rotor with principal moments of inertia of approximately $I_A \sim 6.7 \times 10^{-46}$, $I_B \sim 6.3 \times 10^{-46}$, and $I_C \sim 1.3 \times 10^{-45}$ kg m$^2$ (a planar-ring approximation). Since $I_A$ and $I_B$ have similar values, the behavior of TMO approximately resembles that of an oblate symmetric rotor. The rotational dynamics expected from its principal moments of inertia and the assumption that it behaves as an oblate symmetric rotor (Chan et al. 1960) are consistent with the behavior modeled from experimental EISFs. Thus at $T < 50$ K, TMO performs rotations about the axis with moment of inertia $I_C$, nearly parallel to $C_{2v}$. At higher temperatures, TMO performs a combination of in-plane rotations about an axis perpendicular to the plane of the molecule and rotations about an axis nearly parallel to $C_{2v}$. This combination of several types of rotational motions may increase the probability of coupling with the vibrations of the host lattice. This picture of the rotational motions of TMO and their temperature dependence is also reasonable in light of the low activation energy barriers for the rotation of TMO. That there are no appreciable energy barriers to rotation is tantamount to the absence of strong guest-host interactions in this clathrate hydrate. A strikingly different picture of rotational dynamics is expected for the sI CH of TMO, where steric hindrance plays a role across a wide range of temperature.

## ACKNOWLEDGMENTS

This work utilized facilities supported in part by the National Science Foundation under agreement no. DMR-0086210. The authors thank D. Neumann, L. Saiz, C. Brown, and J. Copley for their comments.

## REFERENCES CITED

Baumert, J., Gutt, C., Shpakov, V.P., Tse, J.S., Krisch, M., Muller, M., Requardt, H., Klug, D.D., Janssen, S., and Press, W. (2003) Lattice dynamics of methane and xenon hydrate: Observation of symmetry-avoided crossing by experiment and theory. Physical Review B, 68, 174301(7).

Bée, M. (1988) Quasielastic Neutron Scattering, Principles and Applications in Solid State Chemistry, Biology and Materials Sciences. Adam Hilger, Bristol.

——— (1992) A physical insight into the elastic incoherent structure factor. Physica B, 182, 332–336.

Bertie, J.E. and Jacobs, S.M. (1977) Far infrared absorption and rotational vibrations of the guest molecules in structure I clathrate hydrates between 4.3 and 100 K. Canadian Journal of Chemistry, 55, 1777–1785.

——— (1978) Infrared spectra from 300 to 10 cm$^{-1}$ of structure II clathrate hydrates at 4.3 K. Journal of Chemical Physics, 69, 4105–4113.

Chakoumakos, B.C., Rawn, C.J., Rondinone, A.J., Stern, L.A., Circone, S., Kirby, S.H., Ishii, Y., Jones, C.Y., and Toby, B.H. (2003) Temperature dependence of polyhedral cage volumes in clathrate hydrates. Canadian Journal of Physics, 81, 183–189.

Chan, S.I., Zinn, J., Fernandez, J., and Gwinn, W.D. (1960) Trimethylene Oxide. III. Far-Infrared Spectrum and Double-Minimum Vibration. Journal of Chemical Physics, 33, 1643–1655.

Copley, J R.D. and Cook, J.C. (2003) The Disk Chopper Spectrometer at NIST: a new instrument for quasielastic neutron scattering studies. Journal of Chemical Physics, 292, 477–485.

Creswell, R.A. (1975) Molecular structure of oxetane. Molecular Physics, 30, 217–222.

Davidson, D.W. (1973) Clathrate Hydrates. In F. Franks, Ed., Water: A Comprehensive Treatise, vol. 2, p. 115–234. Plenum Press, New York.

Gough, S.R., Hawkins, R.E., Morris, B., and Davidson D.W. (1973) Dielectric properties of some clathrate hydrates of structure II. Journal of Physical Chemistry, 77, 2869–2876.

Gough, S.R., Garg, S.K., and Davidson D.W. (1974) Origin of guest-molecule dipoles in the structure I clathrate hydrate of trimethylene oxide. Chemical Physics, 3, 239–247.

Handa, Y.P., Tse, J.S., Klug, D.D., and Whalley, E. (1991) Pressure-induced phase

transitions in clathrate hydrates. Journal of Chemical Physics, 94, 623–627.
Hawkins, R.E. and Davidson, D.W. (1966) Dielectric relaxation in the clathrate hydrates of some cyclic ethers. Journal of Physical Chemistry, 70, 1889–1894.
Kuratomi, N., Yamamuro, O., Matsuo, T., and Suga, H. (1992) Heat capacity and transition phenomena of structure I and II trimethylene oxide clathrate hydrates. Journal of Thermal Analysis, 38, 1921–1937.
Rigny, P. (1972) Reorientations dans le Cristeaux Moleculaires et Fonctions de Correlation. Physica, 59, 707–721.
Rondinone, A.J., Chakoumakos, B.C., Rawn, C.J., and Ishii, Y. (2003) Neutron diffraction study of structure I and structure II trimethylene oxide clathrate deuterate. Journal of Physical Chemistry B, 107, 6046–6050.
Sargent, D.F. and Calvert, L.D. (1966) Crystallographic data for some new type II clathrate hydrates. Journal of Physical Chemistry, 70, 2689–2691.
Tse, J.S. and White, M.A. (1988) Origin of glassy crystalline behavior in the thermal properties of clathrate hydrates: A thermal conductivity study of tetrahydrofuran hydrate. Journal of Physical Chemistry, 92, 5006–5011.
Tse, J.S., McKinnon,W.R., and Marchi, M. (1987) Thermal expansion of structure I ethylene oxide hydrate. Journal Physical Chemistry, 91, 4188–4193.
Tse, J.S., Shpakov, V.P., Murashov, V.V., and Belosludov, V.R. (1997) The low frequency vibrations in clathrate hydrates. Journal of Chemical Physics, 107, 9721–9724.
Tse, J. S., Shpakov, V.P., Belosludov, V.R., Trouw, F., Handa, Y.P., and Press, W. (2001) Coupling of localized guest vibrations with the lattice modes in clathrate hydrates. Europhysics Letters, 54, 354–360.
von Stackelberg, M. and Meuthen, B. (1958) Feste Gashydrate. VII*) Hydrate wasserlöslicher Äther. Zeitschrift für Elektrochemie, 62, 130–131.
Yamamuro, O., Kuratomi, N., Matsuo, T., and Suga, H. (1993) Dielectric study of KOH-doped acetone and trimethylene oxide clathrate hydrates. Journal of Physics and Chemistry of Solids, 54, 229–235.
Yildirim, T., Gehring, P.M., Neumann, D.A., Eaton, P.E., and Emrick, T. (1999) Neutron-scattering investigation of molecular reorientations in solid cubane. Physical Review B, 60, 314–321.

MANUSCRIPT RECEIVED SEPTEMBER 30, 2004
MANUSCRIPT ACCEPTED APRIL 25, 2004
MANUSCRIPT HANDLED BY BRYAN CHAKOUMAKOS